MICROSCOPY

Microscopy **62(1)**: 3–21 (2013)
doi: 10.1093/jmicro/dfs089

Review

Monochromated STEM with a 30 meV-wide, atom-sized electron probe

Ondrej L. Krivanek[1,2,*], Tracy C. Lovejoy[1], Niklas Dellby[1] and R.W. Carpenter[3]

[1]Nion Company, 1102 8th St., Kirkland, WA 98033, USA, [2]Department of Physics, Arizona State University, Tempe, AZ 85287, USA and [3]LeRoy Eyring Center for Solid State Science and Department of Chemistry/Biochemistry, Arizona State University, Tempe, AZ 85287, USA
*To whom correspondence should be addressed. E-mail: krivanek@nion.com

Abstract The origins and the recent accomplishments of aberration correction in scanning transmission electron microscopy (STEM) are reviewed. It is remembered that the successful correction of imaging aberrations of round lenses owes much to the successful correction of spectrum aberrations achieved in electron energy loss spectrometers 2–3 decades earlier. Two noteworthy examples of the types of STEM investigation that aberration correction has made possible are shown: imaging of single-atom impurities in graphene and analyzing atomic bonding of single atoms by electron energy loss spectroscopy (EELS). Looking towards the future, a new all-magnetic monochromator is described. The monochromator uses several of the principles pioneered in round lens aberration correction, and it employs stabilization schemes that make it immune to variations in the high voltage of the microscope and in the monochromator main prism current. Tests of the monochromator carried out at 60 keV have demonstrated energy resolution as good as 12 meV and monochromated probe size of ~1.2 Å. These results were obtained in separate experiments, but they indicate that the instrument can perform imaging and EELS with an atom-sized probe <30 meV wide in energy, and that an improvement in energy resolution to 10 meV and beyond should be possible in the future.

Keywords scanning transmission electron microscopy, aberration correction, single-atom microscopy, single-atom spectroscopy, electron monochromator, high-energy-resolution electron energy-loss spectroscopy

Received 13 November 2012, accepted 20 November 2012; online 17 January 2013

Introduction

The last decade has witnessed major progress in electron microscopy (EM), much of it due to the successful introduction of aberration correction for round lenses. We can now image single atoms as light as boron by scanning transmission electron microscopy (STEM) annular dark field (ADF) imaging, and we can determine the chemical type of single atoms, using one of three different types of signals: ADF image intensity, electron energy loss (EEL) and X-ray spectra. We can even probe the type of bonding holding the single atom in place, by analyzing the fine structure of EEL spectra of single atoms. The spatial resolution attainable by EM (<1 Å) is now surpassing the resolution attainable by scanning tunneling and atomic force microscopes. On small parts of a sample, EM's ability to analyze matter atom by atom, with 100% efficiency,

can surpass the analytical capabilities of the atom probe. In this paper, we review how these advances came about, and give a couple of key recent examples of the progress. We then describe another important advance presently taking place: combining the ability to probe matter at atomic resolution with meV-level electron energy loss spectroscopy (EELS) resolution.

Aberration correction has improved the performance of electron microscopes in a major way by addressing a fundamental problem: round lenses of the type traditionally employed in EM are far from perfect. The limitations of the lenses were investigated by Scherzer, who proved that regular round lenses cannot be free of major aberrations and showed that the aberrations place a severe limit on the resolution attainable by electron microscopes [1,2]. This was clearly an important problem, and much effort was subsequently focused on trying to overcome the limit by aberration correction. Scherzer himself proposed a practical aberration corrector [3] and later initiated a major effort to build working correctors (Scherzer [4], Koops [5]). Many other researchers joined the quest to improve the resolution of the electron microscope by an aberration corrector: see for instance reviews by Hawkes [6], Rose [7], Krivanek *et al.* [8] and Pennycook [9].

Correctors built between 1950 and ~1990 typically demonstrated the correction principle they used, by being able to null the aberrations they set out to correct. But they did not result in an actual resolution improvement, and the practical goal of improving the resolution of the microscope that the corrector was built for was not attained for some four decades. There were three fundamental reasons for this. One, the increased complexity combined with the finite precision with which a corrector could be built meant that parasitic aberrations such as 3-fold astigmatism and axial coma became much more important, to the point of worsening the resolution of the corrected microscope relative to an uncorrected one. Two, the increased complexity of the total system placed increased demands on power supply stabilities, and these were not fully met until the 1990s. Three, the parasitic aberrations needed new diagnostic procedures to measure them and new optical elements to fix them, and these were also not fully developed until the 1990s.

By the early 1980s, the fact that no successful correctors had been built in over 30 years of trying gave aberration correction an aura of impossibility. This was reinforced by the opinions of some of the pioneers in the field, who expressed doubts about whether aberration correction would ever lead to anything practical (e.g. Delltrap and Hardy [10]). As a result, funding agencies became averse to funding aberration correction projects, and most correction research paused for some 10 years. Fortunately for EM, the pause was not a complete one: work on aberration correction continued in the context of EELS, in which second- and later third- and higher-order-corrected spectrometers and imaging filters continued to improve on the performance of their simpler predecessors.

The first second-order-corrected spectrometer for use in an electron microscope was built by Crewe *et al.* [11]. This spectrometer had the unusual property that the aberration was cancelled in one direction only, and it required a rectangular entrance aperture for optimal operation. Several designs that achieved complete second-order correction of axial aberrations followed later (Parker *et al.* [12], Shuman [13], Tang [14], Isaacson and Scheinfein [15]). Aberration correction in the context of EELS was very worthwhile: it increased the collection angle attainable by spectrometers, at a given energy resolution, by about an order of magnitude. For example, an early spectrometer built by one of the present authors used a magnetic prism with straight edges and had no second-order aberration correction, and was able to achieve an energy resolution of 1 eV (at 100 keV operating energy) only if it used an entrance aperture with a 200 μm diameter (Krivanek [16]). A later version of the spectrometer used a prism with curved edges plus auxiliary sextupoles to provide complete second-order aberration correction and was able to achieve a resolution of better than 0.7 eV with an entrance aperture of a 3 mm diameter (Krivanek and Swann [17]). The most recent such instruments correct aberrations up to fifth order and are capable of reaching a <0.1 eV energy resolution with an entrance aperture >3 mm in diameter (Gubbens *et al.* [18]; see also the Results section below). Similarly, recent

versions of imaging filters initially developed by Rose's group use multipoles to correct aberrations up to third order and are capable of achieving an energy resolution of <50 meV and high values of filter transmissivity (Essers *et al.* [19]).

Designing successful aberration-corrected spectrometers provided two of the present authors with the confidence and the practical knowledge needed to embark on developing a corrector of STEM aberrations. A similar process probably also occurred with members of the Rose group. In any case, in the mid-1990s, three aberration correction projects, two in Heidelberg (Germany) and one in Cambridge (UK), culminated in a practical improvement in the resolution reached by a scanning electron microscope (Zach and Haider [20]), by a STEM (Krivanek *et al.* [21,22]) and by a conventional transmission electron microscope (CTEM, Haider *et al.* [23]). The goal of reaching the best directly interpretable resolution in any electron microscope ever was reached soon after, with an improved STEM corrector [22,24], which produced a sub-Å electron probe when mounted in a VG 501 STEM operated at 120 keV (Batson *et al.* [25]).

The rest of the aberration-correction story is now well known: aberration correction has improved the attainable resolution of both the STEM and the CTEM by 2–3×, and this has opened many new windows for observing the atomic world. In the area of STEM imaging, the attainable resolution has been improved repeatedly (Nellist *et al.* [26], Sawada *et al.* [27,28], Erni *et al.* [29])]. The corrected optics has allowed relatively large beam currents to be packed into atom-sized electron probes, first around 0.1–0.2 nA (e.g. Batson *et al.* [25]), and more recently around 1 nA (Dellby *et al.* [30]). Equally importantly, aberration correction has allowed atomic resolution STEM imaging and analysis to be reached at primary energies lower than 100 keV, and this has resulted in nearly damage-free imaging and spectroscopy of individual atoms (Krivanek *et al.* [31–34], Lovejoy *et al.* [35], Suenaga and Koshino [36], Suenaga *et al.* [37], Zan *et al.* [38], Zhou *et al.* [39,40]).

It is now possible to image single light atoms in very thin samples such as graphene and single heavy atoms in samples as thick as 20 nm, identify the chemical type of the atom by its ADF intensity or by its spectroscopic signature, and analyze its atomic environment by the fine structure of its EEL spectrum. Figures 1 and 2 illustrate such capabilities.

Figure 1 shows ADF images of single atoms of silicon embedded in two different configurations in monolayer graphene: (a) 4-fold, in which the Si atom replaces a C–C pair, and (b) 3-fold, in which it replaces a single C atom. The images were collected at a 60 keV primary energy, in two different ways. Image (a) was acquired in 16 separate scans with a dwell time of 24 µs per pixel each, and the scans were aligned by cross-correlation and added up, with no further processing [39]. Image (b) was acquired in a single scan and then Fourier-filtered to smooth it and to remove probe tails [31,34]. The fact that the impurity atom was Si was ascertained from the ratio in the ADF image intensity of the impurity atom and of the matrix atoms [39], and also verified spectroscopically.

Figure 2 shows EEL spectra obtained from the two types of sites in a separate experiment [41], also at 60 keV. The spectra from single Si atoms embedded in graphene in the 4-fold and the 3-fold configurations are shown Fig. 2a, and theoretical spectra calculated using density functional theory are shown in Fig. 2b. The spectra were acquired while a small window centered on the Si atom was scanned at about TV rate, and the window was continuously re-centered over the Si atom if the atom started wandering away from the center of the field of view. In this way, jumps of the Si atom to a neighboring site in the graphene lattice, which happened several times during the experiment, did not result in 'losing' the atom. The neighboring site was typically equivalent, i.e. there was no change in the atom's environment. (Conversion from a 4-fold site to a 3-fold site (and vice versa) requires the incorporation (ejection) of an extra atom into (out of) the graphene sheet, and this happened only very rarely.) The window area was ~7 times the area of the atom and this meant that contributions to the spectrum of the Si atom were accumulated only for ~14% of the total acquisition time. Nevertheless, when the atoms were tracked for ~200 s, as was done in these experiments, spectra with an effective exposure time of ~30 s for the single atoms were obtained.

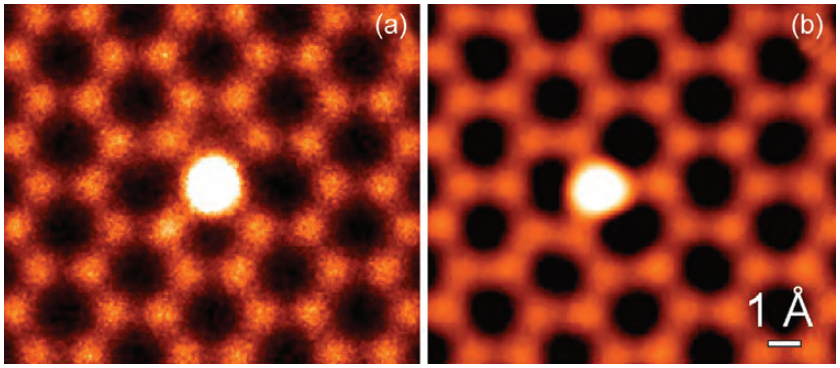

Fig. 1. ADF STEM images of single Si atoms embedded in monolayer graphene. (a) Si in a 4-fold site, replacing two C atoms. (b) Si in a 3-fold site, replacing a single C atom. Courtesy Wu Zhou and Matthew Chisholm (see references [39] and [34]).

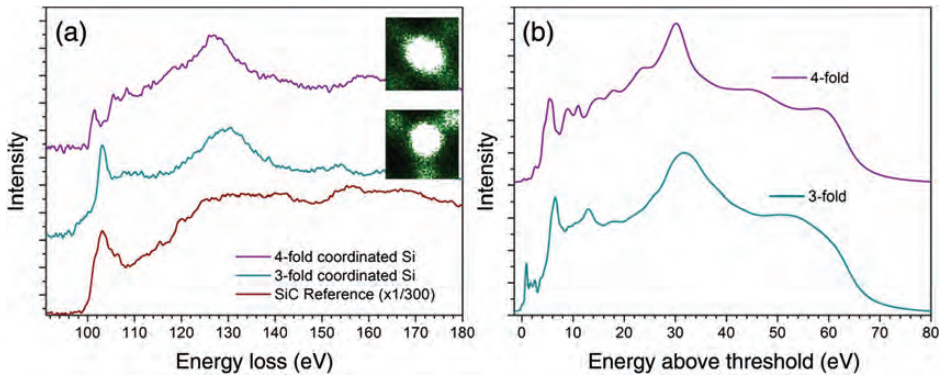

Fig. 2. EEL spectra from the two types of individual Si substitutional atoms and from SiC. (a) Experimental spectra. (b) Simulations. The insets in (a) show the tracking windows used to keep the illumination centered over the atom of interest. Courtesy Quentin Ramasse (see reference [41]).

The beam current was ~50 pA and the beam diameter ~1.2 Å. This meant that the single-atom spectra were obtained with a dose of the order of 10^{10} electrons delivered to each atom. It resulted in EEL spectra of the single Si atoms (which also included a contribution from C atoms in the tracking area) with an intensity of $\sim 10^5$ electrons per eV near the $L_{2,3}$ edge maximum at ~130 eV, of which some 5×10^4 e^-/eV were the net $L_{2,3}$ counts. A single-atom spectrum of this type has a statistical noise of only ~1% root mean square (r.m.s.) even after background subtraction, and this is indeed what is found in the spectra shown in Fig. 2a.

The comparison of the three experimental spectra (Si in a 4-fold site, Si in a 3-fold site and a thin foil of SiC) shows major differences, especially between the two single-atom spectra. The comparison with the theory is excellent for the 4-fold Si and good for the 3-fold Si, for which the calculation has fitted the main experimental features well, but has also produced weak but sharp additional peaks, not observed experimentally, at 1 eV and 13 eV above the edge threshold.

Similar spectra from the two types of Si impurity sites in graphene have been acquired and analyzed by Zhou *et al.* [40]. Their data were acquired as spectrum-images, without using the tracking technique. The number of 60 keV electrons delivered to each Si atom was $\sim 10^9$ and the spectra, therefore, included more statistical noise than the spectra of Fig. 2, but they were acquired from unique sites, without the atoms hopping to neighboring ones. Zhou *et al.*'s analysis showed that Si atoms in the 3-fold sites stick up above the graphene plane and their bonding involves sp^3 hybridization, whereas Si atoms in the 4-fold sites sit in the graphene plane and their bonding involves sp^2d hybridization, in broad agreement with the conclusions of the study by Ramasse *et al.* [41].

The above results demonstrate the advanced state of the development of aberration-corrected STEM

and EELS very effectively. Spectra from single atoms can be obtained with good counting statistics in a few seconds, using an electron beam energy that produces little damage even in a low Z material. Theoretical simulations are capable of reproducing the spectra with a high degree of accuracy. Because atoms are the basic building blocks of matter, it is clear that imaging and analysis in the STEM can now reach, in favorable cases, as fundamental a level of exploration as matter itself allows. It is also clear that an experimental technique that can examine individual atoms one by one is not limited to looking at single atoms and is in fact even more powerful when exploring the properties of the assemblies of atoms that constitute solid materials.

Further accounts of the history of aberration-corrected STEM and of its recent achievements can be found in the comprehensive book edited by Pennycook and Nellist [42] and in the issue of Ultramicroscopy dedicated to Albert Crewe, the inventor of the modern STEM (Isaacson and Krivanek [43]).

Given the major advances that have taken place in the spatial resolution and analytical capabilities that electron microscopes have been able to reach in the last decade, it seems timely to ask: 'Are similar improvements attainable in other aspects of EM and spectroscopy?' One promising avenue is the correction of chromatic aberrations (e.g. Rose and Wan [44]), which is now typically limiting the resolution of electron microscopes more than geometric aberrations, especially at low primary energies.

An even more promising avenue, in our opinion, concerns improving the energy resolution of EELS carried out with atom-sized electron probes. Currently, this technique is capable of reaching about a 40 meV energy resolution for short exposures of the order of 0.1 s and ~70 meV for longer exposures (Essers *et al.* [19]), at a spatial resolution of 0.3–1 nm. These limits are not fundamental, and much new information about many different types of samples would become available if the resolution could be improved to 10–30 meV, especially if combined with an atom-sized probe. For instance, information about energy *gains* in the sample (Boersch *et al.* [45], García de Abajo and Kociak [46]) and even vibrational properties of the sample (optical phonons, Geiger *et al.* [47], Geiger [48]) should become available.

In a previous publication, we have described the theoretical design of a new type of electron monochromator that should be able to reach such a level of performance (Krivanek *et al.* [49]). In this paper, we show the first results obtained with a newly constructed practical implementation of the monochromator, and we discuss the ultimate limits that our approach should be able to reach.

Methods

The images and spectra presented in this paper were acquired with three different Nion UltraSTEM™ scanning transmission electron microscopes. Two of them, located at the Oak Ridge National Laboratory and at the Daresbury SuperSTEM laboratory, had the regular UltraSTEM™ configuration. The third one was the 100 keV monochromated UltraSTEM™ 100MC built for Arizona State University and was located at Nion, where it was undergoing final preshipment tests.

The UltraSTEM™ has been described previously (Dellby *et al.* [30], Krivanek *et al.* [50]). The experiments were carried out mostly at 60 keV, an operating energy that allows the formation of atom-sized electron probes and at the same time stays comfortably below the knock-on threshold for perfect graphene as well as many graphene defects. Two more reasons for favoring 60 keV operation were that scattering cross-sections become larger at lower operating energies and that good energy resolution becomes easier to reach. The beam current was generally between ~10 and 200 pA, i.e. less than the coherent beam current (Krivanek *et al.* [33,51]) of the microscope's cold field emission gun (CFEG), which was typically around 300 pA. The energy spread of the CFEG was around 0.35 eV, a value that permitted the formation of electron probes of a diameter of ~120 pm and a current of 100 pA (at 60 keV).

Two energy loss spectrometers were employed: the Gatan Enfina with optics similar to that of Gatan parallel electron energy loss spectrometers (PEELS) (Krivanek *et al.* [52]), which produced the results shown in Fig. 2, and the Gatan Enfinium,

with optics similar to that of Gatan Quantum (Gubbens *et al.* [18]), which was used for all the other EELS results shown in this paper.

Figure 3 shows a cross-section of an entire UltraSTEM column comprising the recently constructed monochromator (Krivanek *et al.* [53]). Figure 4 shows the monochromator part of the column in greater detail. The monochromator is preceded by two round lenses (ML1, ML2) and a monochromator aperture (MOA) module. The two lenses plus the aperture produce a beam of suitable angular range in the entrance plane of the monochromator, with a beam crossover typically ~10 nm in size appearing at the height expected by the monochromator. The microscope column above the monochromator is very similar to the regular UltraSTEM™ column. It has three condenser lenses plus a virtual objective aperture (VOA) module, a C_3/C_5 aberration corrector and all the other elements of a regular UltraSTEM™. The monochromator plus the extra lens and aperture modules add 48 cm to the total height of the column.

The monochromator (Fig. 4) consists of 21 separate optical layers. Layers 4, 9, 13 and 18 contain magnetic prisms, which together bend the beam by 360°, such that the final beam ends up travelling along the same axis as the incoming beam. The resultant trajectory resembles the Greek letter alpha, and the monochromator can thus be called 'alpha-type'. The electron beam crosses itself in the middle of the prism 4/18. The average distance between electrons in a 60 keV, 1 nA beam is 21 mm, and the chances that an electron in such a beam will experience a significant change in its trajectory by scattering from another electron in the crossing region are negligibly small.

All prisms have straight edges at 90° to the beam. The main prism (layers 4/18) bends the beam by 75°. It has a uniform magnetic field and thus focuses the beam in the dispersion plane only. The

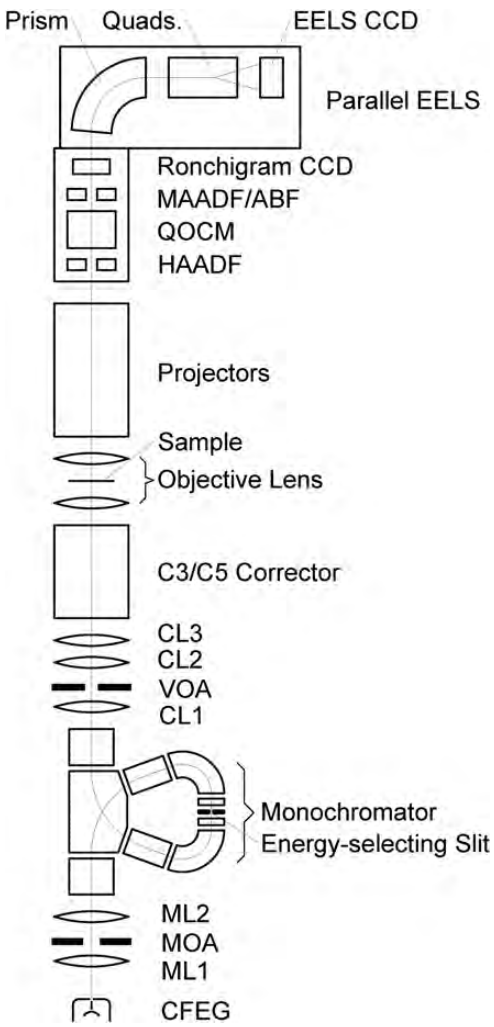

Fig. 3. Schematic cross-section of the monochromated column (Nion UltraSTEM™ 100MC).

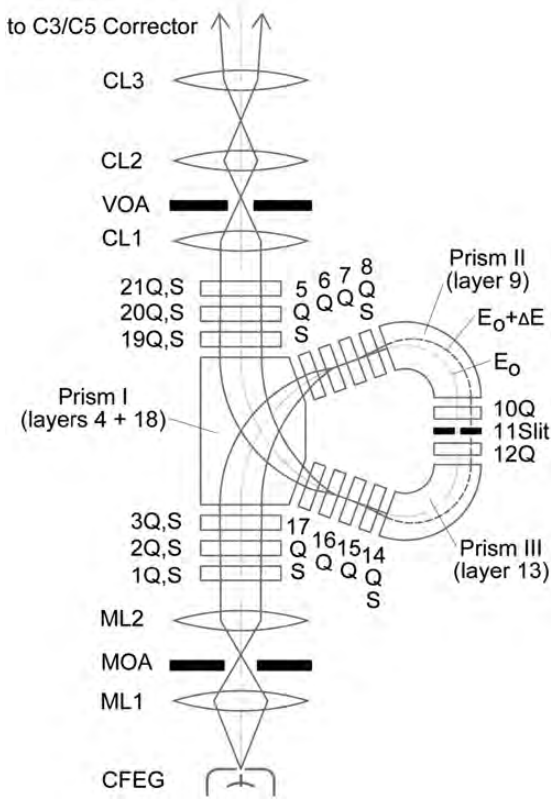

Fig. 4. Schematic cross-section of the monochromator part of the column.

auxiliary prisms (layers 9 and 13) each bend the beam by 105°. They are gradient prisms and give nearly equal focusing in the dispersion and non-dispersion directions. Adjustable magnification and first-, second- and higher order focusing are provided by multipoles in layers 1–3, 5–8, 10, 12, 14–17 and 19–21. The multipoles in these layers typically consist of a strong quadrupole, a sextuple and an octupole, and also weak auxiliary dipoles.

Acting together, the multipoles allow the energy dispersion at the energy selecting slit, located in layer 11, to be adjusted, roughly over the range 3–200 µm per eV at a 60 keV primary energy. They also make sure that the precise symmetry conditions needing to be met at the slit (Krivanek *et al.* [49]) are fulfilled and that second- and third-order aberrations at the slit and also in the beam re-entering the column are either eliminated or suitably minimized.

A simplified understanding of the monochromator can be obtained by regarding it as two parallel electron energy loss spectrometers (PEELS, Krivanek et al. [52]) arranged back-to-back: the first PEELS produces a dispersed and magnified electron energy-loss spectrum at the energy-selecting slit in the center plane, the energy-selecting slit admits a portion of the spectrum into the rest of the apparatus, and the second PEELS, through which the electrons run 'backwards', un-disperses the electron beam and re-inserts it in the microscope column.

The electrons have the full beam energy when they are passing through the monochromator. This brings several important advantages and one disadvantage. The first advantage is that because the electrons are travelling fast, the average separation between them is increased, and the time they spend next to each other is decreased. This plus the fact that the beam is apertured down to nearly the final beam current by the pre-monochromator aperture (MOA) means that stochastic Coulomb interactions (collisional broadening, frequently also called the 'Boersch' effect) in the monochromator are minimized, thus largely preserving the original beam brightness. Second, because the electrons are at the full energy, their sensitivity to local charging, for instance due to contamination at the slit edges, is smaller than if their energy was a few hundred eV. Third, because the beam is not accelerated on leaving the monochromator, the energy selected by the monochromator is independent of the high tension (HT) supplied to the gun, and therefore it is not changed by potentially detrimental effects such as an instability in the HT at the HT generation frequency. Fourth and probably the most important, with the electrons traversing the monochromator and the spectrometer at their full energy, stability-enhancing schemes can be devised and implemented such that:

(a) instabilities in the power supplies of the prisms of the monochromator or of the prism of the spectrometer do not result in shifts of the spectrum on the EELS detector, and

(b) instabilities in the high voltage of the electron source do not result in the spectrum produced at the energy-selecting slit shifting and thus changing the intensity admitted through the slit.

The stabilization of the spectrum on the EELS detector is achieved simply by connecting the principal windings of all the magnetic prisms of the entire monochromated instrument in series, i.e. by passing one and the same supply current through all of them. This makes sure that non-negligible changes in the energy selected by the monochromator, which arise when the current changes by amounts as small as one part in 10^8, are precisely compensated for in the spectrometer, and the spectrum on the detector therefore does not shift. Connecting the prisms of the monochromator in series also essentially eliminates the movement of the probe on the sample, which would otherwise result if the current in an individual prism of the monochromator changed without the same change occurring in all the others. This is important for maintaining high spatial resolution at the sample.

Weak auxiliary windings are provided for each prism to make the prisms individually adjustable. By making sure that the auxiliary fields remain below 1% of the main field, the instabilities due to the auxiliary power supplies become >100 times less important than if all the prism fields were produced by independent power supplies.

The second stabilization is implemented by sensing the current falling on the two halves of the monochromator slit, comparing the two signals in a

feedback circuit connected to the fast control loop of the HT and adjusting the HT so that the two signals remain the same. If this stabilization is turned off, the dispersed zero-loss peak (ZLP) produced by the first half of the monochromator shifts by small amounts relative to its central position on the slit. Because the microscope's CFEG produces a narrow energy distribution, a shift of the ZLP of as little as 50 meV would result in the beam admitted through the slit varying in intensity. The variation would typically produce bright and dark bands in scanned images and other time-resolved data, and these are avoided when the stabilization is turned on.

Taken together, the two stabilization schemes mean that our system is immune to instabilities in essentially the same way as systems that place both the monochromator and the spectrometer at the high voltage potential. A 3 meV energy resolution has been reached with the Boersch/Geiger system employing such a stabilization and operating at 30 keV (Geiger [48]) and 12 meV has been reached with a microscope-based system using similar principles and operating at 60 keV (Terauchi *et al.* [54]). The results section of this paper shows that the present stabilization scheme is capable of leading to similar energy resolution values. Because our system uses a bright CFEG and preserves as much brightness as possible by cancelling the energy dispersion in the beam exiting the monochromator, it is also capable of producing a monochromated electron probe of narrow energy width that is smaller than 2 Å. Neither of the previous high-energy resolution systems was able to produce such a probe.

The chief disadvantage of monochromating at the full beam energy is that the energy dispersion imparted onto the electron beam by the main prism (layer 4/18), whose bending radius is 115 mm, is rather small: 1 μm per eV for a 60 keV beam. The contribution of the second prism (layer 9) to the energy dispersion is even smaller. This means that the spectrum produced by the main prism has to be magnified to give enough dispersion at the slit, so that selecting down to 10 meV energy range can be done with an energy-selecting slit not much narrower than 1 μm, which implies that dispersions of up to 100 μm eV^{-1} may be needed. Such dispersions are readily produced by the quadrupoles in layers 5–8.

After traversing quadrupoles 5–8, the energy-dispersed beam is bent and focused by prism 9 such that it travels downwards at the slit 11. Rays of different energies need to be precisely parallel to each other at the slit, and this is fine-tuned by quadrupole 10. The beam at the slit is focused into a crossover both in the dispersion direction and perpendicular to it. The above conditions satisfy the symmetry requirements that allow the entire monochromator to produce zero energy dispersion at its exit. The second half of the monochromator is operated at almost the same settings as the first half, with small deviations compensating for the departures from exact symmetry that are inescapable with any actual mechanical embodiment.

The primary spectrum of the monochromator, which is produced by the main prism 4/18, is essentially an energy-dispersed image of the source. The size of the source image divided by the energy dispersion poses a fundamental limit on the energy resolution of the monochromator. The source image can be made larger or smaller by exciting lenses ML1 and ML2 differently and by changing the settings of the quadrupoles in layers 1–3. The pre-prism optics is typically adjusted so that the MOA admits $\sim$ 0.5 nA of beam current into the monochromator, and the source image in the primary spectrum is a few nm in size. The energy dispersion of the primary spectrum is $\sim$1 nm per meV and this means that the energy resolution limit due to the finite source size typically amounts to a few meV.

The source image is magnified by quadrupoles 5–8, along with the primary spectrum. It reaches the size of a few tens of nm at the slit when the dispersion at the slit is 10 μm per eV and a few hundreds of nm when the dispersion is 100 μm per eV. This is small enough so that an energy interval as narrow as a few meV can be selected in principle by the slit in our design.

The crossover is demagnified by the second half of the monochromator, which also nulls the energy dispersion. The beam then enters the condenser section of the microscope in much the same way as the unmonochromated beam produced by the electron gun enters the condenser section of a regular UltraSTEM™. The post-monochromator column in the present instrument is essentially the same as in the regular Nion UltraSTEM™ [50], and the

condenser and corrector sections of the monochromated instrument are operated much like in its unmonochromated cousin.

The angular range of the beam, which was originally defined by the MOA, is re-defined by the VOA situated between condenser lenses CL1 and CL2. This step is necessary because the VOA plane contains a diffraction pattern due to the slit, and this causes the MOA image to become distorted when the monochromator slit is made narrow. Moreover, to change the current in the sample-level probe, we adjust the condenser section of the column to change the source demagnification. This results in the image of the MOA, as projected onto the Ronchigram CCD, changing relative to the size of the VOA. As in the unmonochromated column, the probe angle defined by the VOA typically needs to be set to the largest admissible angle compatible with the aberration characteristics of the probe-forming column, and the angle remains nearly constant from day to day. In normal operation of the instrument, the MOA image appearing on the Ronchigram CCD is between ~1.1× and 5× larger than the VOA image. The nearly equal aperture size ratio gives the largest probe current.

An increased size of the projected source leads to a worsened spatial resolution. This cannot be avoided when monochromation is being pushed to its energy resolution limits and a substantial beam current is needed at the same time. The same kind of compromise is familiar to all users of STEMs: optimizing for a high spatial resolution means that the probe current needs to be restricted; optimizing for a sizeable beam current means that the spatial resolution grows worse. When monochromating as well, either the spatial or the energy resolution requirements (or both) need to be relaxed if the beam current value is to remain in the useful range for spectroscopy (typically 50 pA and above).

The vacuum inside the monochromator is sealed only with metal seals (Cu gaskets and C-rings). The whole monochromator is bakeable to 140°C, and it has its own ion pump that is mounted in the 'pumping tree' of the UltraSTEM™. The monochromator produces no appreciable extra gas load entering the rest of the column. Because the monochromator is situated between the CFEG, which needs extreme ultra-high vacuum (UHV), and the sample, which is best surrounded by a clean (hydrocarbon-free) and dry (moisture free) UHV, making sure that it does not produce an extra gas load is essential.

The monochromator contains many further elements whose full description would require more space than available in this paper. These include sensing apertures that allow the beam to be detected even if it is so misaligned that it cannot traverse the whole monochromator, a CCD camera lens-coupled to a scintillator which can temporarily replace the slit, actuators that allow the slit width to be adjusted as needed or the slit to be removed from the beam altogether or replaced by the scintillator, a sensitive arrangement for detecting the beam currents falling on the two slit halves, 4 layers of magnetic shielding and an extra layer of thermal shielding. Provision has been made for water-cooling of the main dispersion-magnifying (and demagnifying) quadrupole assemblies, which can each generate a heat load of a few Watts when the dispersion at the slit is near its maximum.

The main prism has two equal windings that can be run either in parallel or in opposition. For operation of the microscope without monochromation, the polarity of one of the two windings is switched. This results in the field in the prism being cancelled and the electron beam progressing straight up the column, without the heat load changing. Another way to dispense with the monochromation is to keep the electron trajectories through the monochromator unchanged, but to withdraw the slit from the beam.

A more thorough description of the entire monochromated system and its different operation modes will be provided in a separate publication.

Monochromator results

The initial testing of the monochromator proceeded in steps that followed the beam as it progressed through the system, i.e. first through the main prism 4/18, then through quadrupoles 5–8, prism 9, and then through the rest of the system. During the incremental testing phase, we took advantage of the modular nature of the Nion microscope and mounted the monochromator in the projector lens section of the microscope column, where it was easier to put on and take off and where the vacuum

requirements were less severe than nearer the gun. The primary purpose of these tests was to make sure that the monochromator optics had worked out as designed, and that it was able to produce, at the energy-selecting slit, a high-quality spectrum of the energy distribution of the primary beam.

Figure 5 shows a spectrum recorded during the tests, at 100 keV primary energy, with a fiber-optically coupled CCD camera temporarily replacing the energy-selecting slit. The CFEG emission current was ~0.5 μA. The spectrum shows the energy width expected for (310) W CFEG running at a reduced emission current. It also shows the asymmetry characteristic of CFEG sources.

In normal operation of the monochromator, the slit selects a part of the energy distribution, and which exact part is selected determines the intensity of the beam exiting the monochromator. Figure 5 makes it clear that if, for instance, the selected energy interval shifted from the peak maximum to negative ΔE (higher absolute energy) by just 100 meV, the current admitted through the slit would drop to ~50%. In our system, this kind of fluctuation is prevented by the feedback scheme that senses the slit current. One should also note that in order for the selected energy interval to be narrower than the energy width of the CFEG energy distribution, the energy resolution of the first half of the monochromator must be much better than this width. In other words, the energy resolution requirements placed on the monochromator are much more stringent that 0.25 eV.

Figure 6 explores the ultimate energy resolution attainable with our system. It shows ZLPs obtained with a Gatan Enfinium spectrometer, and the monochromator mounted in the correct position between the gun and the condenser lenses and running as a full monochromator. The dispersion at the slit was only ~10 μm per eV but even so the slit was made narrower than 10 meV (judged by the intensity reduction of the beam). A 300 μm diameter aperture was used in the entrance plane of the EELS so that the monochromator and spectrometer aberrations would not need to be adjusted very accurately. The energy calibration was characterized by changing the voltage applied to the drift tube of the EELS prism and was accurate to ~1%. The spectra were obtained by rapid acquisition with only 0.11 ms per spectrum and then integrating 20 spectra for the fast spectrum and 500 spectra for the slower one. This meant that the acquisition time was 2 ms for (a) and 55 ms for (b). The spectra were not aligned in energy before they were added up, so that the broadening of the spectrum resolution with longer acquisition time would be correctly simulated.

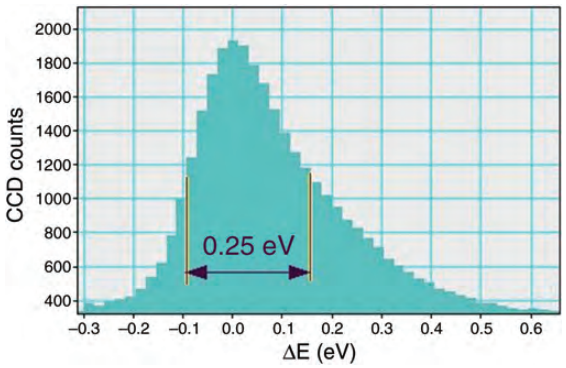

Fig. 5. The energy distribution of the primary beam captured with a CCD camera replacing the monochromator slit.

The 2 ms spectrum ZLP has a full-width at a half-maximum (FWHM) of 12 meV. In the 55 ms acquisition (spanning over three cycles of the mains alternating current (AC) frequency), the FWHM has broadened to ~16 meV. In spectra acquired in 1 s and longer, the FWHM is typically broadened further to 20–30 meV. Nevertheless, the potential energy resolution of our instrument is clearly similar to the results obtained with Terauchi *et al.*'s system [54], and it is likely to improve further as we improve the stability performance and gain more experience with optimizing the adjustment of the system.

Figure 7 explores the quality of aberration correction in the monochromator and in the spectrometer at larger spectrometer acceptance angles. It shows a pair of images of the ZLP, as detected on the EELS CCD, displaced by 100 meV applied to the EELS prism drift tube. The diameter of the EELS entrance aperture was 3 mm, and this was about the same size as the unscattered beam, which spanned ±27 mr at the sample. In other words, approximately the full beam incident on the sample was admitted into the spectrometer. The fact that the ZLP lines are straight and narrow and that the tails of the ZLP are highly suppressed (see Fig. 7b) shows that the optics of the monochromator and

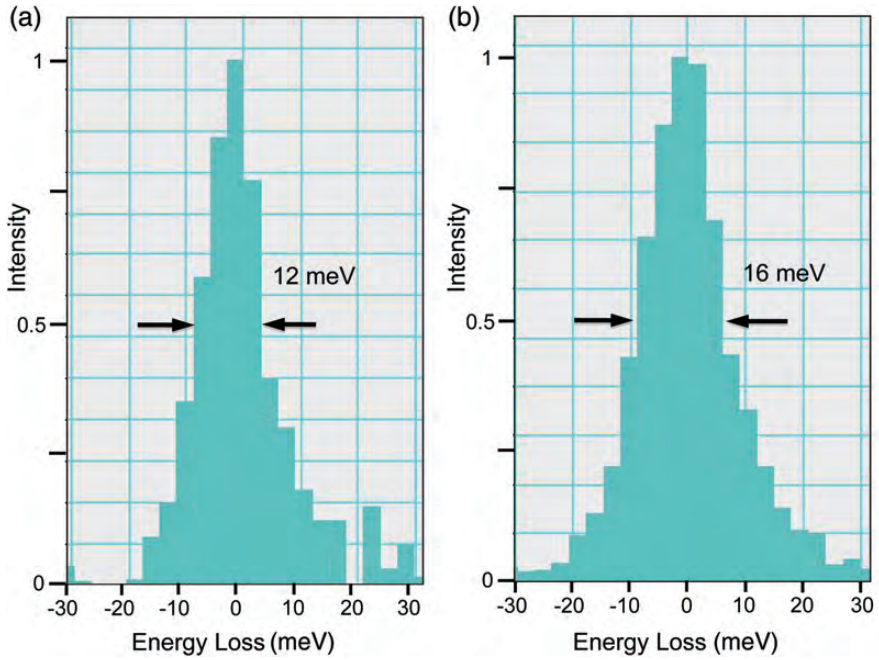

Fig. 6. Monochromated ZLPs recorded with a Gatan Enfinium spectrometer at 60 keV. The exposure time was 2 ms for (a) and 55 ms for (b). The energy dispersion was 3 meV per channel.

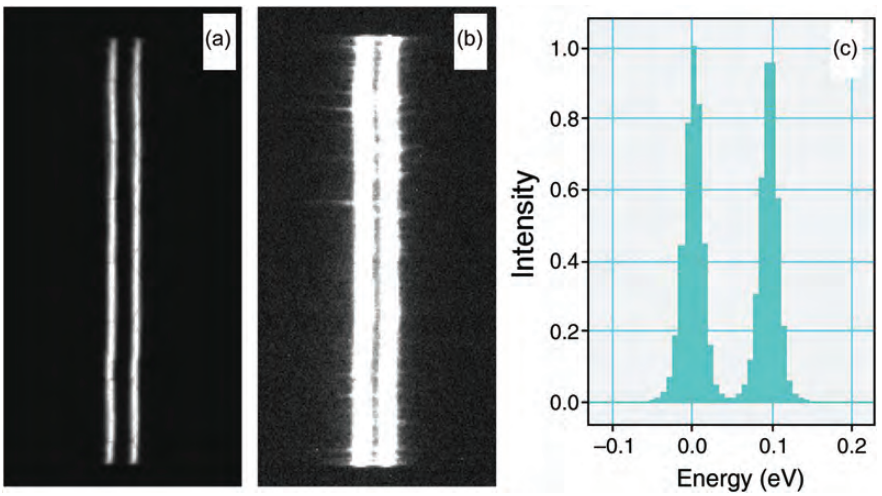

Fig. 7. Images of the ZLP as detected on the EELS CCD. Two peaks are recorded, displaced by 0.1 eV. (a) The double image printed with regular contrast and showing the FWHM. (b) The same image printed much brighter (2% of maximum intensity = white) showing the tails of the ZLPs. (c) Integrated profiles (integrated along the length of the ZLP lines).

that of the spectrometer are compatible with ~20 meV FWHM EELS resolution at close to a 100% collection efficiency and that the ZLP tails can be controlled with about a ±20 meV precision (with some small exceptions due to the charging at the edges of the EELS entrance aperture, since replaced by a better quality one). In order to achieve this performance, multipoles in the spectrometer up to the dodecapole were all excited, for nearly complete 4-th order correction and partial fifth order correction. There were typically 4 controls per aberration order up to fourth order plus just the principal fifth order control, i.e. a total of 17 controls.

We have not yet fully investigated the electron-optical coupling of the spectrometer to the microscope column, and using shorter camera lengths at the EELS entrance aperture may turn out to be capable of coupling even higher sample-level angles

into the spectrometer without a significant energy resolution loss.

It is useful to note that when observing the ZLP, small departures from monochromaticity arising in the monochromator, i.e. different angular segments of the beam at the monochromator exit corresponding to slightly different electron energies, can be compensated by the spectrometer such that at the EELS detector, the image of the ZLP appears undistorted. Looking at the ZLP recorded by the spectrometer when the slit is almost fully closed, the effects of small optical adjustments made to the monochromator and to the spectrometer appear very similar.

However, scattering by the sample redistributes the electrons in the angular space, and departures from monochromaticity at the sample become mixed in such a way that they cannot be unmixed by the spectrometer. Moreover, departures from monochromaticity in the probe illuminating the sample lead to an increase in the size of the probe. The second effect arises because the probe size is inversely proportional to the transverse size of the electron wave packet as defined by the VOA. If the VOA is illuminated by an electron beam whose energy varies across the aperture, then the size of the wave packet describing each individual electron is limited by this variation: the electron wave cannot traverse the VOA in places where electrons of its energy are not admitted. (Another way of thinking about this phenomenon is that when the beam is not precisely focused into a crossover at the monochromator slit, an image of the slit appears superposed on the image of the VOA.) When such a misadjustment occurs, the VOA-level wave packets become smaller (in the energy dispersion direction), and this leads to a corresponding increase in the beam size at the sample. This means that the VOA needs to be illuminated by a beam of uniform energy, and a non-negligible loss of spatial resolution is incurred if the monochromator tuning is not precise enough to achieve this.

In order to address the two effects described above, we have developed a Ronchigram-based tuning procedure that optimizes the spatial resolution by fine-tuning the monochromator's isochromaticity. In other words, the procedure allows us to separate monochromator tuning from spectrometer tuning. It is now being automated, and it will be described in a future publication.

Exploring the energy resolution that should be obtainable with longer exposure times in our system in the future, Fig. 8 shows two time-resolved traces of the zero-loss position on the CCD detector of the EELS. Trace (a) was obtained by double-focusing the spectrum on the CCD and reading it out continuously, at 0.11 ms per line. It initially showed a 60 Hz modulation of an amplitude of ~15 meV, and this was removed by adjusting the EELS AC compensation control. The remaining short-term instabilities then became largely aperiodic, with a peak-to-peak magnitude of ~10 meV (on a time scale of tens of ms). Trace (b) was generated by acquiring a time sequence of 1200 spectra of 2 ms

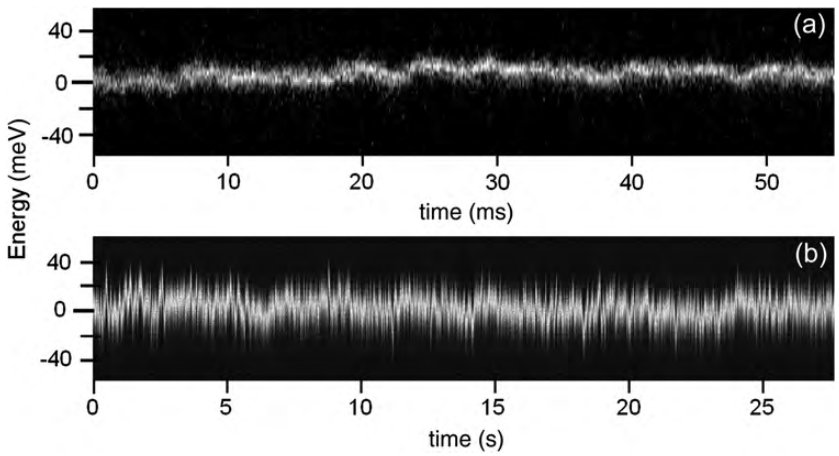

Fig. 8. Time-resolved traces of the ZLP position on the CCD detector showing time-dependent instabilities. (a) Instabilities over 55 ms. (b) Instabilities over 28 s.

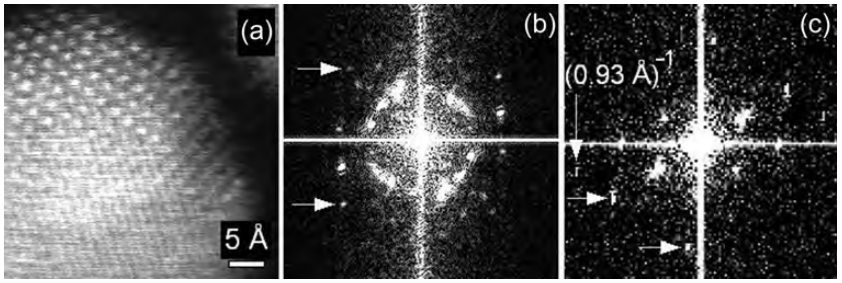

Fig. 9. STEM ADF images of Au nanoparticles recorded at 60 keV and their Fourier transforms. (a) Monochromator on, slit withdrawn. (b) Fourier transform of an Au nanoparticle in (a). (c) Fourier transform of an Au nanoparticle in a similar ADF image taken with the slit inserted and set to ~100 meV width. The horizontal arrows point to $(1.23\ \text{Å})^{-1}$ Fourier transform reflections, the vertical arrow points to a $(0.93\ \text{Å})^{-1}$ reflection.

each, spread over 32 s, and collating them into a time-energy image. The medium-term instabilities (time scale of 0.25 s and above) that the trace documents are also largely aperiodic, with a peak-to-peak magnitude of ~40 meV and hence ~10 meV r.m.s. deviations. Longer-term instabilities were also analyzed, by acquiring spectra over several minutes (not shown here). They demonstrated that the long-term drift was typically <5 meV per min. This resulted in the energy resolution in spectra recorded in 100 s being nearly the same as the resolution in spectra recorded in 1 s.

Because the short- and medium-term instabilities come from neither the prism current variation nor variations in the high voltage, we should be able to decrease them significantly, once we have identified their precise source. Possible causes include mechanical vibrations of the EEL spectrometer, instabilities of the deflectors in the post-sample part of the Nion column, and instabilities in the EELS multipole and the EELS drift tube power supplies. The stability required of the EELS multipole supplies is rather high and there are many of them, because the Enfinium uses a separate power supply for each pole of its seven 12-pole optical elements. The tests of Fig. 8 were carried out with Gatan's extra-high stability power supplies (originally developed for the high-voltage version of the Quantum imaging filter), but even so it is likely that a further improvement in this area will be required if resolution of 10 meV is to be reached for acquisition times of 0.1 s and longer, particularly at 100 or 200 keV primary energy.

The measured long-term drift was better than expected, especially in view of the relatively unstable environment in the assembly/testing area at Nion. For comparison, the HT of the microscope can easily drift by ~100 mV in 5 min if the room temperature is changing, and there are also shorter-term peak-to-peak instabilities of up to ~100 mV. The measured stability values of the total instrument therefore show that our two stabilization schemes are working well.

Figure 9 explores the spatial resolution obtainable with our system when monochromating. The main figure (Fig. 9a) shows a part of an ADF STEM image of Au nanoparticles on amorphous carbon, obtained with the beam passing through the monochromator and the slit retracted. The Fourier transform (Fig. 9b) shows strong transfer of spatial frequencies up to $(1.23\ \text{Å})^{-1}$ (Au (222) reflection), which indicates that even with its considerably more complicated optical trajectory, the monochromated system is behaving similarly to Nion UltraSTEMs not equipped with a monochromator. Figure 9c shows the Fourier transform of a Au particle obtained with the slit inserted and adjusted to ~100 meV energy width. It contains strong transfer at $(1.23\ \text{Å})^{-1}$ and also a weaker transfer at $(0.93\ \text{Å})^{-1}$ (Au (331) reflection). The beam current was ~120 pA for (a) and (b) and 10 pA for (c), for which the source size was demagnified more.

An improvement in the resolution of the monochromated image is expected on theoretical grounds: the spatial resolution should become *better* as the energy width of the beam is decreased, because the resolution limit due to chromatic effects becomes less important. However, for this to be observed in practice, many things have to be done right: the tuning of the isochromaticity at the VOA aperture must be very precise, the tuning of

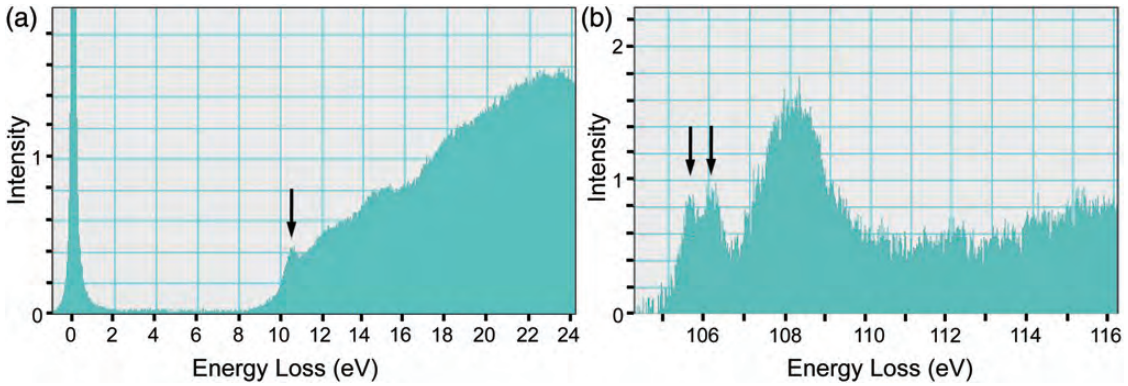

Fig. 10. Si spectra from SiO_2 in a MOSFET integrated circuit. (a) Low loss spectrum acquired in 0.2 s. (b) Background-subtracted Si $L_{2,3}$ edge acquired in 50 s.

geometric aberrations of the probe at the sample must be more precise for the monochromated case than the unmonochromated one, sufficient beam brightness must be preserved even when monochromating, the energy-selecting slit must not distort the image of the source unduly, and there must be no major instabilities resulting from the monochromator operation. To our knowledge, Fig. 9 is the first experimental demonstration that all these potential difficulties can be overcome, and the STEM's spatial resolution can be either maintained or improved when monochromating.

Figure 10 shows spectra acquired at 60 keV from a practical sample: an SiO_2 layer in an integrated circuit comprising nanoscale metal-oxide-semiconductor field-effect transistors (MOSFETs). The illuminating beam was spread to ~2 nm diameter, in order to minimize the radiation damage. Figure 10a shows an unprocessed (apart from gain normalization) low loss spectrum, Fig. 10b shows a gain-normalized and background-subtracted Si $L_{2,3}$ edge. The energy dispersion was 20 meV per channel, so that a range of 40 eV would be covered by the 2048-channel EELS CCD. The ZLP (not shown at its full height) was ~40 meV wide at half-maximum, i.e. only 2 energy channels wide. This was possible because of the high spatial resolution of the scintillator used by the CCD.

The ZLP intensity was 302 on the intensity scale of the low-loss spectrum. The intensity of the low-loss features is between ~0.1 and 1.6 on this scale, which means that if the low-loss features are not to be obscured by the tail of the ZLP, its suppression is very important. This has been accomplished quite effectively: at an intensity level of 3.0, i.e. at 1% of full height of the ZLP, the peak was 0.2 eV wide, and at a 0.3 intensity (0.1% of the ZLP), it was ~0.7 eV wide. A significant portion of the observed tail intensity arose by re-scattering, in the scintillator and the coupling fiber-optics, of the electrons and photons properly belonging to the ZLP. We plan to look into ways of eliminating this contribution in the future.

The contribution of the ZLP tail to the low-loss spectrum can of course also be decreased by increasing the dispersion on the EELS CCD. At a dispersion of 0.56 meV per channel, the measured ZLP intensity was reduced to 0.1% of its peak value at 80 meV energy loss and to 0.01% at 170 meV energy loss. This represents about a 3-fold narrowing of the ZLP tail relative to values reported previously (Essers *et al.* [19]).

Despite the ZLP tail present in Fig. 10a, the 'insulator gap' in the spectrum intensity between the ZLP and ~9 eV is very clearly visible. The low-loss spectrum shows an interesting sharp feature at ~10.5 eV (arrowed), which may be due to a band edge exciton (Batson [55]). The $L_{2,3}$ spectrum shows a double peak at the threshold of the edge, at ~106 eV, split by 0.6 eV (also arrowed). This corresponds to the Si $L_{2,3}$ edge spin-orbit splitting, and has been observed before (Batson [56]), but not with as good an energy resolution as here. The acquisition times were 0.2 s for (a) and 50 s for (b). The long acquisition time for the $L_{2,3}$ spectrum was necessary partly because we did not optimize the

beam current in the electron probe and also because the slit was only ~10 meV wide.

The results of Fig. 10 were obtained in a single experimental session. They were not meant to be an in-depth study of the MOSFET device, but rather to show that many new and interesting experimental results will be obtainable with our instrument.

Discussion

Despite the limited practical experience we have had with the monochromated STEM system so far (~ 4 months of testing of the complete system), it is clear that our expectations for its performance have been largely fulfilled. The stabilization schemes have worked out very much as we had hoped, and the instabilities we have seen so far should be straightforward to overcome. The optics has also largely worked out as expected. We have been able to obtain very good energy resolution, and to keep and even slightly improve the STEM spatial resolution when monochromating.

Our two stabilization schemes make the system immune to instabilities in the high voltage, which is hard to stabilize to better than ~3 parts in 10^7 with present-day electronics over a time scale of a few seconds (~60 mV at 200 kV and 20 mV at 60 kV), and two to three times these values over a few minutes. They also make it immune to instabilities in the prism current, which can be reduced to <1 in 10^8 for time periods shorter than 1 s, but whose longer term drifts can easily reach one part in 10^7, and thus a 20 meV shift of a 100 keV ZLP if the stabilization is not implemented (note that $\Delta E/E_0 \sim 2\ \Delta I/I_0$, where ΔE is the energy change and ΔI the current change). The remaining instabilities that affect the energy resolution of our system for longer acquisition times are due to deflections of the beam occurring between the energy-selecting slit and the EELS detector.

Because the probe at the sample needs to be kept stable to within a fraction of 1 Å, the main part of the microscope column has already been made largely immune to such deflections. However, in the detector section of the column, instabilities amounting to an EEL spectrum jitter of few tens of meV are not readily noticeable when operating without a monochromator, at ~0.3 eV resolution. As a result, the detector part of the column and the EELS itself are normally not designed to the same standards. For example, the mu-metal shielding of the detection column and of the EELS tend to be single rather than double (or triple or even quadrupole, as used in some parts of the probe-forming column), and the beam is allowed to become much wider (and hence more sensitive to stray fields and other instabilities) in the detector and the EELS sections than in any other part of the column. Moreover, instability-minimizing precautions employed in the pre-sample microscope column (including the monochromator and the corrector), such as decreasing the range of deflector coils to the minimum possible value, are not always employed, especially in the EELS. None of this is surprising: up to now, there was no need to make these parts of the column as stable as the probe-forming part. The relaxed standards are the primary reason for the instabilities we have observed so far. Removing them will mean that the detector column and the EELS will have to be brought up to the same standards as the rest of the microscope.

When the instabilities are brought down to ~3 meV r.m.s. and below, a 10 meV energy resolution is likely to become available for examining real samples, rather than for a demonstration of the potential performance of the system, as was done with the 12 meV resolution spectrum here. Moreover, with a substantially improved energy stability, more precise tuning of the monochromator and of the spectrometer should become possible. This should in turn lead to an energy resolution even better than 10 meV, which will be very useful for vibrational spectroscopy, similar to the work of Geiger *et al.* [47,48], but at a much higher spatial resolution. We intend to pursue such a direction in future stages of this project.

Another important aspect for the optimum operation of a monochromated STEM system will be the brightness of the electron gun, best measured by the gun's coherent probe current I_c [33,51], normalized by the energy width ∂E of the electron source as $I_{cn} = I_c/\partial E$. Present-day CFEGs have an energy width of ~0.3 eV, and typically give normalized coherent currents I_{cn} of 0.5–1 nA eV^{-1}. This is ~5 times higher than what is possible even with the brightest Schottky sources, whose energy width

is round 1 eV. 1 nA eV^{-1} is very adequate for achieving atom-sized electrons probes with >100 pA of current in all non-monochromated STEM applications and also for monochromated applications down to an energy resolution of ~50 meV. With the monochromator slit closed even further and selecting as little as 1% of the incident beam (for a 3 meV wide selection window), however, I_{cn} much larger than 1 nA eV^{-1} would be very useful. It will be interesting to see whether new sources that increase the I_{cn} value substantially can be developed in the future.

Quantitative estimates of the attainable probe size indicate that with a CFEG producing $I_{cn} = 0.5$ nA eV^{-1}, atomic resolution (<2 Å) should be reachable at 100 keV, in theory, at a beam current of 100 pA and an energy width of 20 meV. Decreasing the beam energy width to around 10 meV is likely to mean having to relax the spatial resolution, probably to around 3 Å at a current of 100 pA. Attaining such high current values will require that the semi-angle of the probe be opened up to ~50 mrad, a value permitted by the decreased importance of the energy spread of the monochromated beam. This will then place higher demands on the quality of the correction of geometric aberrations in the monochromator, the probe-forming optics and the spectrometer, and it may take some time before it is attained in practice. With the optics optimally adjusted, it should then also be possible to form 2 Å, 20–50 pA, 10 meV wide probes.

In closing the discussion section, it is interesting to note that the overall concept of the monochromator described in this paper was proposed by two of the present authors over 20 years ago (Krivanek *et al.* [57]) and that the present design is greatly enhanced relative to the original proposal (as described in this paper and also in Krivanek *et al.* [53] and Krivanek and Dellby [58]). In the original design, the monochromator was not a dispersing–undispersing one. This would have entailed a major loss of beam brightness, beyond the loss that is unavoidable when a narrow pass-band of energies is selected. Second, the original design made no provision for increasing the dispersion of the spectrum at the energy-selecting slit beyond the dispersion produced by a combination of magnetic prisms, and the dispersion would thus have been too small to provide high energy resolution. Third, unlike the present system, the optics of the originally proposed monochromator did not include the elements necessary for complete second- and third-order aberration correction.

As a fourth and rather separate point, there was no provision for the correction of chromatic aberration (C_c) of the probe-forming optics, whereas the present monochromator design includes the possibility of correcting C_c by magnetic-only means, with the energy-selecting slit removed from the beam [49,58]. Preliminary tests have shown that the correction principle is sound, but also that the trajectories through the monochromator that work best for monochromating and for C_c correction are substantially different and that the switchover from one to the other requires a retuning of the monochromator, which is not yet fully automated. The correction approach should lead to improved spatial resolution at the full beam current, with no change in the energy resolution relative to the unmonochromated beam. It will be interesting to compare it with the alternative approach to higher spatial resolution possible with our system, which was illustrated by Fig. 9: decreasing the energy spread of the incident beam to around 100 meV and hence giving up some 2/3 of the potentially available probe current, but improving the energy resolution at the same time as improving the spatial resolution.

Conclusions

The Nion monochromator represents a return to the beginnings of our journey through the electron optics landscape. Having started with the design of electron spectrometers and imaging filters and having then progressed to aberration correction of probe-forming optics, we are now working on optimizing the energy resolution of an entire STEM-EELS system. We bring to the task the experience gained while working on aberration correction and whole-microscope design.

The new system's performance promises to be a fundamental leap forward relative to our beginnings in EELS and also a major step forward relative to existing STEM-EELS systems. The development has followed the usual path of progress in science, as

recently illustrated by Howie for the case of EM [59]: an upward spiral that revisits places the field has been at previously, but typically at a significantly higher level.

A truly optimized high-energy and high-spatial-resolution monochromated energy-analyzing STEM system will require:

(a) an electron source with the highest possible value of the normalized coherent probe current,
(b) a monochromator with aberration-corrected optics,
(c) highly aberration-corrected probe-forming optics,
(d) an EEL spectrometer with highly corrected optics and very good stabilities,
(e) a linking scheme between the monochromator and the spectrometer that makes the recorded spectra immune to principal instabilities in either system,
(f) a stabilization scheme that makes the whole system immune to instabilities in the high voltage,
(g) power supplies and multipole arrangements with the best possible stabilities throughout the system,
(h) minimization of stochastic Coulomb broadening (Boersch) effects in the monochromator, and
(i) largely automated operation.

Our present design makes a fundamentally new start on this road. The design is capable of providing 20 – 30 meV energy resolution with an atom-sized electron probe already now, and it will most likely progress to an energy resolution of ~10 meV with an atom-sized probe in forthcoming stages of our project. The road is wide open, and further improvements in both the system performance and the range of potential applications are likely. It promises to be a paradigm-changing development, and an exciting and worthwhile journey for those who embark on it.

Funding

Financial support was provided by National Science Foundation grant DMR MRI #0821796 (awarded to Arizona State University), by National Science Foundation grant DMR MRI-R2 #959905 (awarded to Rutgers University), Department of Energy grant DE-SC0007694 (awarded to Nion Company), UK Engineering and Physical Research Council for capital equipment grant (EP/J021156/1, awarded to the SuperSTEM National Facility For Aberration Corrected STEM at Daresbury Labs), Arizona State University, Rutgers University and Nion Co.

Acknowledgements

We are grateful to Matthew Chisholm, Juan-Carlos Idrobo, Quentin Ramasse and Wu Zhou for permission to show their results, to our present and past co-workers at Nion, especially George Corbin, Neil Bacon, Petr Hrncirik, Nathan Kurz, Matthew Murfitt, Jon Nelson, Gwyn Skone, Jonathan Ursin and Zoltan Szilagyi for their help with various aspects of the monochromated system, to Phil Batson for discussions and general collaboration, to Phil Batson, Rik Brydson, Peter Nellist, Quentin Ramasse and Mervyn Shannon for their confidence that Nion will be able to design and deliver a high performance STEM-EELS system, to John Bruley for lending us a MOSFET sample, and to Ray Egerton and Peter Rez for discussions about vibrational spectroscopy. Our thanks also go to Sander Gubbens, Yu Sato, Colin Trevor, and Ray Twesten of Gatan for help with optimizing the Enfinium spectrometer, for a loan of extra-high stability power supplies, and for an instability-analyzing script (provided by CT).

References

1 Scherzer O (1936) Über einige Fehler von Elektronenlinsen. *Z. Physik.* **101**: 593–603.
2 Scherzer O (1949) The theoretical resolution limit of the electron microscope. *J. Appl. Phys.* **20**: 20–29.
3 Scherzer O (1947) Sphärische und chromatische Korrektur von Elektronenlinsen. *Optik* **2**: 114–132.
4 Scherzer O (1978) Limitations for the resolving power of electron microscopes. In: Sturgess J M (ed.), *Electron Microscopy 1978*, **Vol. 3**, pp 123–129 (Microscopical Society of Canada, Toronto).
5 Koops H (1978) Aberration correction in electron microscopy. In: Sturgess J M (ed.), *Electron Microscopy 1978*, **Vol. 3**, pp 185–196. (Microscopical Society of Canada, Toronto).
6 Hawkes P W (2007) Aberration correction. In: Hawkes P W and Spence J C H (eds), *Science of Microscopy*, pp 696–747 (Springer, New York and Berlin).
7 Rose H (2003) Advances in electron optics. In: Ernst F and Rühle M (eds), *High Resolution Imaging and Spectrometry of Materials*, pp 189–270 (Springer, Berlin and New York).
8 Krivanek O L, Dellby N, and Murfitt M F (2009) Aberration correction in electron microscopy. In: Orloff J (ed.), *Handbook of Charged-Particle Optics*, pp 601–640 (CRC Press, Boca Raton).
9 Pennycook S J (2011) A scan through the history of STEM. In: Pennycook S J and Nellist P D (eds), *Scanning Transmission Electron Microscopy: Imaging and Analysis*, pp 1–90 (Springer, New York).
10 Delltrap J H M and Hardy D F (2003) Private communication.
11 Crewe A V, Isaacson M, and Johnson D (1971) A high resolution electron spectrometer for use in transmission scanning electron microscopy. *Rev. Sci. Instrum.* **42**: 411–420.
12 Parker N W, Utlaut M, and Isaacson M S (1978) Design of magnetic spectrometers with second order aberrations corrected. I: Theory. *Optik* **51**: 333–351.

13 Shuman H (1980) Correction of the second-order aberrations of uniform field magnetic sectors. *Ultramicroscopy* **5**: 45–53.

14 Tang T T (1982) Design of an electron spectrometer for scanning transmission electron microscope (STEM). In: Johari O (ed.), *Scanning Electron Microscopy*, Part 1, pp 39–50 (SEM Inc., A M F. O'Hare, Chicago, IL).

15 Isaacson M and Scheinfein M (1983) A high performance electron energy loss spectrometer for use with a dedicated STEM. *J. Vac. Sci. Technol.* **B1**: 1338–1343.

16 Krivanek O L (1979) Design of a compact, medium resolution electron energy loss spectrometer. In: Proceedings 37th EMSA meet, pp 530–531.

17 Krivanek O L and Swann P R (1981) An advanced electron energy loss spectrometer. In: Proceedings of Quantitative Microanalysis with High Spatial Resolution, pp 136–140 (The Metals Society, Bristol).

18 Gubbens A J, Barfels M, Trevor C, Twesten R, Mooney P E, Thomas P, Menon N K, Kraus B, Mao C, and McGinn B (2010) The GIF Quantum, a next generation post-column imaging energy filter. *Ultramicroscopy* **110**: 962–970.

19 Essers E, Benner G, Mandler T, Meyer S, Mittmann D, Schnell M, and Höschen R (2010) Energy resolution of an omega-type monochromator and imaging properties of the MANDOLINE filter. *Ultramicroscopy* **110**: 971–980.

20 Zach J and Haider M (1995) Aberration correction in a low-voltage SEM by a multipole corrector. *Nucl. Instrum. Methods A* **365**: 316–325.

21 Krivanek O L, Dellby N, Spence A J, Camps R A, and Brown L M (1997) Aberration correction in the STEM. *Inst. Phys. Conf. Ser.* **153**: 35–40.

22 Krivanek O L, Dellby N, and Lupini A R (1999) Towards sub-Å electron beams. *Ultramicroscopy* **78**: 1–11.

23 Haider M, Uhlemann S, Schwan E, Rose H, Kabius B, and Urban K (1998) Electron microscopy image enhanced. *Nature* **392**: 768–769.

24 Dellby N, Krivanek O L, Nellist P D, Batson P E, and Lupini A R (2001) Progress in aberration-corrected scanning transmission electron microscopy. *J. Electron Microsc.* **50**: 177–185.

25 Batson P E, Dellby N, and Krivanek O L (2002) Sub-Ångstrom resolution using aberration corrected electron optics. *Nature* **418**: 617–620.

26 Nellist P D, Chisholm M F, Dellby N, Krivanek O L, Murfitt M F, Szilagyi Z S, Lupini A R, Borisevich A, Sides W H, and Pennycook S J (2004) Direct sub-angstrom imaging of a crystal lattice. *Science* **305**: 1741–1742.

27 Sawada H, Hosokawa F, Kaneyama T, Ishizawa T, Terao M, Kawazoe M, Sannomiya T, Tomita T, Kondo Y, Tanaka T, Oshima Y, Tanishiro Y, Yamamoto N, and Takayanagi K (2007) Achieving 63 pm resolution in scanning transmission electron microscope with spherical aberration corrector. *Jap. J. Appl. Phys.* **46**: L568–L570.

28 Sawada H, Tanishiro Y, Ohashi N, Tomita T, Hosokawa F, Kaneyama T, Kondo Y, and Takayanagi K (2009) STEM imaging of 47-pm-separated atomic columns by a spherical aberration-corrected electron microscope with a 300-kV cold field emission gun. *J. Electron Microsc.* **58**: 357–361.

29 Erni R, Rossell M D, Kisielowski C, and Dahmen U (2009) Atomic-resolution imaging with a sub-50-pm electron probe. *Phys. Rev. Lett.* **102**: 096101.

30 Dellby N, Bacon N J, Hrncirik P, Murfitt M F, Skone G S, Szilagyi Z S, and Krivanek O L (2011) Dedicated STEM for 200 to 40 keV operation. *Europ. Phys. J. Appl. Phys.* **54**: 33505.

31 Krivanek O L, Dellby N, Murfitt M F, Chisholm M F, Pennycook T J, Suenaga K, and Nicolosi V (2010) Gentle STEM: ADF imaging and EELS at low primary energies. *Ultramicroscopy* **110**: 935–945.

32 Krivanek O L, Chisholm M F, Nicolosi V, Pennycook T J, Corbin G J, Dellby N, Murfitt M F, Own C S, Szilagyi Z S, Oxley M P, Pantelides S T, and Pennycook S J (2010) Atom-by-atom structural and chemical analysis by annular dark-field electron microscopy. *Nature* **464**: 571–574. (see also the on-line supplementary information at http://www.nature.com/nature/journal/v464/n7288/suppinfo/nature08879.html).

33 Krivanek O L, Zhou W, Chisholm M F, Dellby N, Lovejoy T C, Ramasse Q M, and Idrobo J C (2012) Gentle STEM of single atoms: low keV imaging and analysis at ultimate detection limits. In: Bell D C and Erdman N (eds), *Low Voltage Electron Microscopy: Principles and Applications*, pp 119–161 (Royal Microscopical Society, London).

34 Krivanek O L, Chisholm M F, Murfitt M F, and Dellby N (2012) Scanning transmission electron microscopy: Albert Crewe's vision and beyond. *Ultramicroscopy* **123**: 90–98.

35 Lovejoy T C, Ramasse Q M, Falke M, Kaeppel A, Terborg R, Zan R, Dellby N, and Krivanek O L (2012) Single atom identification by energy dispersive x-ray spectroscopy. *Appl. Phys. Lett.* **100**: 154101.

36 Suenaga K and Koshino M (2010) Atom-by-atom spectroscopy at graphene edge. *Nature* **468**: 1088–1090.

37 Suenaga K, Okazaki K, Okunishi E, and Matsumura S (2012) Detection of photons emitted from single erbium atoms in energy-dispersive X-ray. *Nat. Photonics* **6**: 545–548.

38 Zan R, Ramasse Q M, Bangert U, and Novoselov K S (2012) Graphene Reknits Its Holes. *Nano Lett.* **12**: 3936–3940.

39 Zhou W, Oxley M P, Lupini A R, Krivanek O L, Pennycook S J, and Idrobo J-C (2012) Single atom microscopy. *Microsc. Microanal.* **18**: 1342–1354.

40 Zhou W, Kapetanakis M D, Prange M P, Pantelides S T, Pennycook S J, and Idrobo J-C (2012) Direct determination of distinct atomic configurations and bonding of individual impurities in graphene. *Phys. Rev. Lett.* **109**: 206803.

41 Ramasse Q M, Seabourne C R, Zan R, Kepaptsoglou D-M, Bangert U, and Scott J A (2012) Probing the bonding and electronic structure of single atom dopants in graphene with electron energy loss spectroscopy. *Nano Lett.* DOI: 10.1021/nl304187e.

42 Pennycook S J and Nellist P D (eds) (2011) *Scanning Transmission Electron Microscopy: Imaging and Analysis*. (Springer, New York).

43 Isaacson M S and Krivanek O L (eds) (2012) *Commemorative issue dedicated to Albert Crewe. Ultramicroscopy*: **123**.

44 Rose H and Wan W (2005) Aberration correction in electron microscopy. In: Proceedings of 2005 Particle Accelerator Conference, pp 44–48 (Knoxville, Tennessee), also available at: accelconf.web.cern.ch/accelconf/p05/PAPERS/WOAC001.PDF.

45 Boersch H, Geiger J, and Stickel W (1966) Interaction of 25-keV electrons with lattice vibrations in LiF. Experimental evidence for surface modes of lattice vibration. *Phys. Rev. Lett.* **17**: 379–381.

46 García de Abajo F J and Kociak M (2008) Electron energy-gain spectroscopy. *New J. Phys.* **10**: 073035.

47 Geiger J, Katterwe H, and Schröder B (1971) Electron energy loss spectra of graphite single crystals and evaporated carbon films in the range 0.02–0.4 eV. *Z. Physik.* **241**: 45–54.

48 Geiger J (1981) Inelastic electron scattering with energy losses in the meV-region. In: Bailey G W (ed.), *Proc. 39th EMSA Meeting*, pp 182–185 (Claitors, Baton Rouge, LA, USA).

49 Krivanek O L, Ursin J P, Bacon N J, Corbin G J, Dellby N, Hrncirik P, Murfitt M F, Own C S, and Szilagyi Z S (2009) High-energy-resolution monochromator for aberration-corrected scanning transmission electron microscopy/electron energy-loss spectroscopy. *Phil. Trans. R. Soc. A* **367**: 3683–3697.

50 Krivanek O L, Dellby N, Keyse R J, Murfitt M F, Own C S, and Szilagyi Z S (2008) An electron microscope for the aberration-corrected era. *Ultramicroscopy* **108**: 179–195.

51 Krivanek O L, Chisholm M F, Dellby N, and Murfitt M F (2011) *Atomic-resolution STEM at low primary energies*. In: Pennycook S J and Nellist P D (eds), *Scanning Transmission Electron Microscopy: Imaging and Analysis*, pp 613–656 (Springer, New York).

52 Krivanek O L, Ahn C C, and Keeney R B (1987) Parallel detection electron spectrometer using quadrupole lenses. *Ultramicroscopy* **22**: 103–116.

53 Krivanek O L, Lovejoy T C, Corbin G J, Dellby N, Murfitt M F, Kurz N, Batson P E, and Carpenter R W (2012) Monochromated STEM with high energy and spatial resolutions. *Microsc. Microanal.* **18**: (Suppl. 2) 330–331.

54 Terauchi M, Tanaka M, Tsuno K, and Ishida M (1999) Development of a high energy-resolution electron energy loss spectroscopy microscope. *J. Microsc.* **194**: 203–209.

55 Batson P E (2012) Private communication.

56 Batson P E (1996) Atomic resolution electronic structure in silicon-based semiconductors. *J. Electron Microsc.* **45**: 51–58.

57 Krivanek O L, Gubbens A J, and Dellby N (1991) Developments in EELS instrumentation for spectroscopy and imaging. *Microsc. Microanal. Microstruct.* **2**: 315–332.

58 Krivanek O L and Dellby N (2010) High resolution energy-selecting electron beam apparatus. US patent application 20120074315.

59 Howie A (2012) Learning from past epiphanies, successes and disappointments to anticipate future progress in microscopy. *Micros. Microanal.* **18** (Suppl. 2): 1948–1949.